Lawrence Berkeley National Laboratory
LBL Publications

Title

XFEL Microcrystallography of Self-Assembling Silver n-Alkanethiolates.

Permalink

https://escholarship.org/uc/item/5xj129qd

Journal

Journal of the American Chemical Society, 145(31)

Authors

Aleksich, Mariya
Paley, Daniel
Schriber, Elyse
et al.

Publication Date

2023-08-09

DOI

10.1021/jacs.3c02183

Peer reviewed

eScholarship.org Powered by the California Digital Library
University of California

Author Manuscript

Author Manuscript

Author Manuscript

Author Manuscript

HHS Public Access

Author manuscript

J Am Chem Soc. Author manuscript; available in PMC 2025 February 12.

Published in final edited form as:

J Am Chem Soc. 2023 August 09; 145(31): 17042–17055. doi:10.1021/jacs.3c02183.

XFEL Microcrystallography of the Self-Assembling Silver *n*-Alkanethiolates

Mariya Aleksich[1,2,¥], **Daniel W. Paley**[6,¥], **Elyse A. Schriber**[1,2,¥], **Will Linthicum**[1,3], **Vanessa Oklejas**[6], **David W. Mittan-Moreau**[6], **Ryan P. Kelly**[1,2], **Patience A. Kotei**[1,2], **Anita Ghodsi**[1], **Raymond G. Sierra**[4], **Andrew Aquila**[4], **Frédéric Poitevin**[4], **Johannes P. Blaschke**[5], **Mohammad Vakili**[7], **Christopher J. Milne**[7], **Fabio Dall'Antonia**[7], **Dmitry Khakhulin**[7], **Fernando Ardana-Lamas**[7], **Frederico Lima**[7], **Joana Valerio**[7], **Huijong Han**[7], **Tamires Gallo**[7,8], **Hazem Yousef**[7], **Oleksii Turkot**[7], **Ivette J. Bermudez Macias**[7], **Thomas Kluyver**[7], **Philipp Schmidt**[7], **Luca Gelisio**[7], **Adam R. Round**[7], **Yifeng Jiang**[7], **Doriana Vinci**[7], **Yohei Uemura**[7], **Marco Kloos**[7], **Mark Hunter**[4], **Adrian P. Mancuso**[7,10,11], **Bryan D. Huey**[1,3], **Lucas R. Parent**[9], **Nicholas K. Sauter**[6], **Aaron S. Brewster**[*,6], **J. Nathan Hohman**[*,1,2]

[1]Institute of Materials Science, University of Connecticut, Storrs CT, USA 06269

[2]Department of Chemistry, University of Connecticut, Storrs CT, USA 06269

[3]Department of Materials Science and Engineering, University of Connecticut, Storrs, CT, USA 06269

[4]Linac Coherent Light Source, SLAC National Accelerator Laboratory, Menlo Park, CA, USA 94025

[5]National Energy Research Scientific Computing Center, Lawrence Berkeley National Laboratory, Berkeley, CA, USA 94720

[6]Molecular Biophysics and Integrated Bioimaging Division, Lawrence Berkeley National Laboratory, Berkeley, CA, USA 94720

[7]European XFEL, Holzkoppel 4, Schenefeld, Germany 22869

[8]MAX IV Laboratory, Lund University, Box 118, SE-22100 Lund, Sweden 221 00

[9]Innovation Partnership Building, University of Connecticut, Storrs CT, USA 06269

[10]Department of Chemistry and Physics, La Trobe University, Melbourne, Australia 3086

[11]Diamond Light Source, Harwell Science & Innovation Campus, Oxfordshire, UK OX11 0QX

Abstract

[*]Corresponding Author: asbrewster@lbl.gov, james.hohman@uconn.edu.
[¥]Denotes Equal Contribution

Supporting Information. Additional images, discussion pertaining to standard reaction enthalpy and molecule length; additional synchrotron powder X-ray diffraction data; SAED analysis and additional discussion, and discussion of systematic absences in smSFX data.

Competing interests: Authors declare no competing interests.

Author Manuscript Author Manuscript Author Manuscript Author Manuscript

New synthetic hybrid materials and their increasing complexity have placed growing demands on crystal growth for single-crystal X-ray diffraction analysis. Unfortunately, not all chemical systems are conducive to the isolation of single crystals for traditional characterization. Here, small-molecule serial femtosecond crystallography (smSFX) at atomic resolution (0.833 Å) is employed to characterize microcrystalline silver *n*-alkanethiolates with various alkyl chain lengths at X-ray free electron laser facilities, resolving long-standing controversies regarding the atomic connectivity and odd-even effects of layer stacking. smSFX provides high-quality crystal structures directly from the powder of the true unknowns, a capability that is particularly useful for systems having notoriously small or defective crystals. We present crystal structures of silver *n*-butanethiolate (C4), silver *n*-hexanethiolate (C6), and silver *n*-nonanethiolate (C9). We show that an odd-even effect originates from the orientation of the terminal methyl group and its role in packing efficiency. We also propose a secondary odd-even effect involving multiple mosaic blocks in the crystals containing even-numbered chains, identified by selected-area electron diffraction measurements. We conclude with a discussion of the merits of the synthetic preparation for the preparation of microdiffraction specimens and compare the long-range order in these crystals to that of self-assembled monolayers.

Graphical Abstract

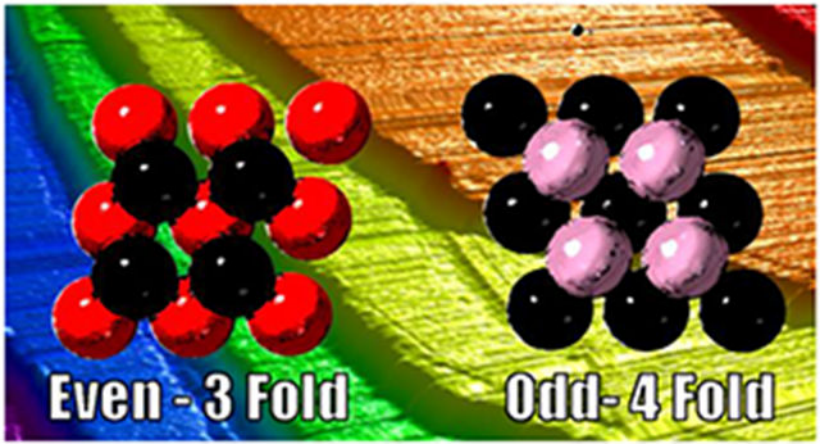

Introduction

Metal-organic chalcogenolates (MOChas) are self-assembling coordination polymers of a metal and an organic source of sulfur, selenium, or tellurium. Recently, compounds in this family have attracted interest for semiconducting properties, light-matter interactions, and catalytic activity.[1,2,3,4,5,6,7,8,9,10,11] The silver *n*-alkanethiolates[12,13,14,15,16] have drawn consistent interest as three-dimensional analogs to the well-studied self-assembled monolayers on silver and gold metal surfaces[17] and for their antimicrobial activity.[18] However, a lack of single crystal structure because of small crystal sizes is a common refrain in reports of these and related compounds. Recently, we used small-molecule serial femtosecond X-ray crystallography (smSFX) to circumvent crystal growth challenges by performing serial crystallography directly on micro- and nano-crystalline powders in liquid phase injection media, without dehydration and vacuum exposure. We found linear

Author Manuscript Author Manuscript Author Manuscript Author Manuscript

Ag-Ag argentophilic interactions[19] in the inorganic layer of silver benzenethiolate with tetracoordinate sulfur bridging chains.[20] We postulated that such argentophilic interactions were also important in the silver *n*-alkanethiolates, so we determined to resolve outstanding questions using the smSFX technique. Following the introduction of high-energy (15-18 keV) data collection at the X-ray free electron laser (XFEL) light sources, Linac Coherent Light Source (LCLS) and European XFEL (EuXFEL), we developed new computational methods to reliably determine unit cells and full crystal structures of several silver *n*-alkanethiolates at the standard 0.833 Å resolution for chemical crystallography.

In seminal work, Dance et. al. first reported a variety of layered nonmolecular silver organothiolates.[21] More recently, with growing interest in two-dimensional (2D) inorganic systems, renewed interest in these compounds has emerged with studies of phase behavior and reports of a high degree of similarity between materials having different alkyl chain lengths.[22,23] Complementary examples of copper, gold, and cadmium *n*-alkanethiolates and thiocyanates have been reported.[1,2,24]

Although the layered motif of the silver *n*-alkanethiolates is well-accepted, the details of the structure have been subject to considerable study and speculation. Dance proposed a reasonable quasihexagonal inorganic lattice for silver benzenethiolate that formed the starting point for future inquiry,[21] and this model was adopted by Fijolek *et al.* for the silver *n*-butanethiolate.[25] A modified form of this model having hexagonally arranged silver atoms with sulfur in a bridging configuration was later proposed in Bensebaa *et al.*[13] Allen and coworkers reported an odd-even effect in layer thickness where packing efficiency appears related to whether the alkyl chain in question has an odd or even number of carbon atoms.[22,23] In addition to disagreement over the atomic connectivities of the inorganic component, the lattice type, alkyl chain tilt angle, and space group have all been controversial.

We synthesized silver *n*-alkanethiolates of varying alkyl chain length (AgS-R; R= C_2H_5 – $C_{12}H_{25}$) using a method of direct chalcogenation of the silver oxide by the corresponding *n*-alkanethiol.[26] This approach produces materials ideal for characterization by smSFX, transmission electron microscopy (TEM), and atomic force microscopy (AFM). We will present monoclinic crystal structures of silver *n*-butanethiolate (C4), silver *n*-hexanethiolate (C6), and silver *n*-nonanethiolate (C9) solved using smSFX. Additionally, the C9 example was collected to a high degree of redundancy. We then use AFM and TEM to evaluate the molecular organization of the materials. We confirm a combination of high degree of structural conservation with increasing alkyl chain length. The alkyl chains themselves are tilted 22° relative to the normal of the inorganic plane, and linear argentophilic interactions between silver atoms with distances close to the interatomic spacing in silver metal are observed. These results reveal the atomic scale organization of the material family and provide insight into the stacking differences for odd- and even-numbered *n*-alkanethiolate chains.

Author Manuscript Author Manuscript Author Manuscript Author Manuscript

Results and Discussion

Synthesis and Characterization of the Silver *n*-Alkanethiolates

The synthetic procedure and products are depicted in Figure 1. Silver *n*-alkanethiolates are abbreviated in shorthand by their carbon chain length, CX, where X=2-12, corresponding to the number of carbons in the alkyl chain. We prepared each CX by conversion of silver (I) oxide with each respective liquid thiol reagent. Reagent can be supplied neat, or in a small quantity (~1 mL) of solvent. The reaction is shown in equation 1.

$$2\ \mathrm{RSH}\ (l) + \mathrm{Ag_2O}\ (s) \rightarrow 2\ \mathrm{AgSR}\ (s) + \mathrm{H_2O}\ (l)$$

Equation 1:

The reaction (equation 1) is convenient for the preparation of CX microcrystals. The vigor of the reaction is inversely proportional to the length of the alkyl chain, where short molecules react quickly, while longer molecules require considerable applications of heat and additional time. The shortest alkyl chains (C2, C3) produced aggregated products that proved unsuitable for smSFX. We have collected images of those samples in the supplemental figure S1. Mid-length (C5-C7) are the most straightforward preparations and produced usable product in most conditions. Figure 2 presents representative SEM images of the compounds with carbon chain lengths ranging from 4 to 12. Well-formed crystals are tabular rectangles and have two relatively straight and parallel edges. Curved edges are seen most often on the short edges of the rectangles. Crystals are uniformly too-small for single-crystal XRD but are excellent substrates for imaging, surface probe, and smSFX analyses.

For insight into the decrease in reaction vigor with chain length, we calculated the standard reaction enthalpy for the range of products C6-C14, and collected the results in supplemental Figure S2. Conveniently, Levchenko *et. al.* previously reported the enthalpy of formation of silver *n*-alkanethiolates as a function of alkyl chain length,[16] and the enthalpy of formation for *n*-alkanethiols can be estimated by group-contribution models.[27] All of the products we selected for this work have a negative standard reaction enthalpy, but only slightly for C12. This is consistent with our observations of decreasing reaction vigor with chain length and provides insight into why the longer chain systems required prolonged heating and incubation treatments to achieve a complete reaction by this method.

We directed considerable attention to the purity of the CX products and avoided pulverization of microcrystals during purification. *Safety note:* Even though they do not interfere with X-ray sampling in the liquid phase, residual unreacted thiols are odorous and unpleasant and must be removed before safe handling. Product can be recovered from excess thiol by filtration, centrifugation, or sedimentation and decanting. Silver (I) oxide is a crystalline impurity and so can be detected in X-ray diffraction. Example of crystals contaminated by this impurity is shown in Figures 2C9, 2C11, 2C12, manifesting as the small dots adhering to the crystals, and a powder X-ray diffraction (PXRD) characterization of C12 samples with and without silver oxide present is found in supplemental Figure S3. We obtained high-resolution PXRD data at the Advanced Photon Source (APS) BM-11[28]

Author Manuscript Author Manuscript Author Manuscript Author Manuscript

and include those results in the supplemental Figure S4. At the time of the smSFX experiment, we found that residual silver (I) oxide was still contaminating some of the longer-chain samples (C9-C12) prior to smSFX experiments. Serendipitously, the difference in settling rates of the silver oxide is such that it rapidly deposits from suspension in organic alcohols and aqueous detergent solutions, enabling purification by decanting after only a few minutes. We were therefore able to characterize samples by smSFX without damaging crystals by a laborious separation procedure. This method was resilient, enabling smSFX even of residues that arrived for beamtime with an insoluble crystalline contaminant.

Surface Structures and Defects of the Silver Alkanethiolates

Atomic force micrographs of the C9-C12 crystals are collected in Figure 3. Well-resolved step edges of the C12 system are shown in Fig. 3A. Each step edge is on the order of 2.6 nm, corresponding to the thickness of a single layer consisting of two *n*-alkanethiolate moieties and the coordinated silver atoms (Fig. 1D). Figure 3B reveals no systematic differences between crystals of different alkyl chain lengths, other than an increase of step edge height with alkyl chain length. Aside from the occasional step edges, individual crystals appear largely featureless. The lack of identifiable domains of molecules in the CX crystal interfaces is in stark contrast to self-assembled monolayers on gold or silver, wherein differently tilted groupings of molecules adsorbed on those surfaces have recognizable linear boundaries. More interesting features are the curvature and roughness of the step edges, especially near the growth plane.

For context, we briefly consider the domain boundary defects in the standing phases of *n*-alkanethiolate self-assembled monolayers (SAMs) on metallic substrates. We limit our comparison to the standing phase, and not to the lying-down or sitting phases where interdigitation of the alkyl units is an observed motif.[29,30,31] Although SAMs lack the multilayering and the fully oxidized metal component of crystalline CX salts, they both exhibit well-packed alkyl molecules tilted with respect to the attached plane of inorganic atoms.[32] Octadecanethiolate SAMs on Ag{111} have reported tilts of 13° from the normal.[33] and closer to 30° on Au{111}.[34,35,36] The azimuthal tilt domain boundaries are one of the most recognizable features in SAMs and emerge from the relative tilts of molecular domains that have a different azimuth.[37] We found little support for such molecular domains in our images on the CX crystals. The implication of this observation is that the crystals are nominally single-domain on a per layer basis and that individual crystals are considerably uniform in azimuth. This motivated the characterization of the crystals in the following sections, as we were interested in understanding the molecular scale structure, connectivity, and their long-range order.

smSFX Data Collection and Processing

X-ray free electron lasers produce a high-flux pulsed X-ray beam via self-amplified spontaneous emission (SASE). The ultrafast pulse duration (30-50 fs) and the micron focusing optics at most XFEL facilities make them well-suited for serial femtosecond crystallography (SFX) of microcrystals. SFX relies on the concept of “diffraction before destruction” to collect room-temperature diffraction data.[38] The XFEL pulse duration is

Author Manuscript Author Manuscript Author Manuscript Author Manuscript

faster than radiation-induced ionization damage, and the high-photon-flux of each pulse can produce strong diffraction signal from microcrystals.

XFEL measurements result in a dataset of ~10^6 images where typically 1%-10% of images contain diffraction spots. SFX data collection of the silver alkanethiolates was performed at three different experimental beamtimes at LCLS[39] and EuXFEL.[40] Each experiment involves a unique set of parameters that place shifting demands on sample delivery.

Table 1 collects experimental parameters at each experiment. Microcrystals were suspended in a carrier solvent and delivered to the XFEL interaction region by three-dimensionally printed gas dynamic virtual nozzle (GDVN) liquid jet delivery systems.[41,42] Depending on experiment compatibility, crystals were suspended either in organic alcohols (e.g. methanol) or in a 0.1 wt% aqueous solution of household liquid detergent (Dawn™) at crystallite concentrations ranging from 1-4 mg/mL.

We collected screening hits on C3, C4, C6, C7, C8, C9, C10, and C12 at the P216 experiment at LCLS at a lower resolution. We obtained atomically resolved structure solutions on C6 and C9 at the LY65 experiment at LCLS, and subsequently C4 at 3073 at EuXFEL. We were additionally able to obtain preliminary indexing solutions for C7, C8, C10, and C12, indicating single crystal hits and highly similar unit cell parameters aside from the long *b* axis. The aggregates of C3 produced abundant, richly populated hits with typically uninterpretable patterns consistent with the aggregated polycrystalline particles observed in Figure S1.

With data collection complete, the individual frames must be indexed. Sparse diffraction patterns from materials with small unit cells are challenging to derive indexing solutions from, due to the lack of visible periodicity in single, unrotated patterns. Without periodicity, Fourier methods typically used in indexing fail.[43,44] For this reason, we developed an algorithm for indexing sparse patterns that we used recently, and in this work.[45,20] Here, however, the *b* lattice is much longer than the lattice vectors from Schriber 2022, which leads to obvious periodicity. We speculated that this could be enough to lock in a Fourier indexing solution, but one vector appeared insufficient, and indexing failed. Therefore, we again used our sparse pattern indexing methods. A complete description of the steps employed to index and process the datasets is found in the experimental section.

We note that the quality of the indexed C9 data was exceptionally good, yielding a final R1 value of 9.4% for all data within 0.833 Å. The dataset is also exceptionally large with 24522 frames indexable by current methods. This afforded a multiplicity of 135x in the outer shell and 183x overall, making this a valuable dataset for future computational methods development. We have made the full raw dataset (660k frames) available through CXIDB.

Crystal Structures of C4, C6, C9

Crystallographic parameters for the three solved crystal structures of C4, C6, and C9 are collected in Table 2. With the exceptions of packing at the molecular interlayer and alkyl chain length, the structures of the three materials are highly conserved. Cross-sectional views of the CX crystals are collected in Figure 4. We consider first the layered organization

Author Manuscript Author Manuscript Author Manuscript Author Manuscript

of the material, then the atomic configuration of the inorganic silver and sulfur layer orientation. Later we will consider the topic of how this terminal group orientation impacts the interlayer registries.

The monoclinic unit cells contain two antiparallel layers with organic groups projected between them. In agreement with earlier work, we find the three compounds have similar short axes and the long axis is increased by the length of the alkyl chains.[13] The alkyl chains are tilted by 22° with respect to the 2D planes constituted by the silver atoms. The structural models here reveal that molecules are aligned nearly end to end as a consequence of the antiparallel layers. The implications of the difference are detailed in the section on the odd-even effect on interlayer stacking, *vide infra*.

The interesting features of the inorganic layer include the 2D silver layer comprised of thiolate-bridged 1D argentophilic chains. The inorganic connectivities of the three systems are conserved with molecule length, depicted in Figure 4. We find nominally linear chains of silver atoms with short argentophilic interactions at 2.85 Å, quite similar to the interatomic spacing of silver atoms in metallic silver metal.[46,19] The Ag-Ag bonding axis is parallel to (101), bisecting the *a* and *c* axes. The Ag-Ag spacing from chain to chain is at least 3.6 Å, generally considered out of range for Ag-Ag interactions. The silver pattern is reminiscent of our earlier report of a linear Ag-Ag motif in silver benzenethiolate; here we found the same nominally linear arrangement of 1D Ag-Ag bonding with longer interchain spacings and lower sulfur coordination.

Selected Area Electron Diffraction

We next employed selected area electron diffraction (SAED) with a TEM to measure the orientation of the observed crystals and determine the relationship between molecular azimuth and crystal habit. Crystals tend to have a preferred orientation on the TEM grid, conveniently enabling electron diffraction through the methyl-terminated basal plane with observation down the *b* axis (<010> zone axis). As shown (Fig. 4a,c,e) the alkyl chains are inclined 22° to this viewing axis.

Figure 5 depicts bright-field TEM (a-d) and diffraction (e-h) characterization for C9-C12, respectively. The crystal fast growth direction is aligned to the *a* axis. Because the unit cell is monoclinic, *a* is not aligned with *a**, as noted in the figure. A complete description of the nomenclature is provided in the supporting information that serves to clarify the complexities of interpreting SAED results in the context of monoclinic unit cells. The alkyl chain azimuth (purple arrows, Fig. 4b,c,f) is nearly aligned to *a** and *-a** in alternating layers. The azimuth is defined by the vector overlapping the alkyl chain projected onto the inorganic plane, with measured values of [1 0 .24], [1 0 .25] and [1 0 .23] for C4, C6, and C9. These values imply that the azimuthal projection is closely conserved regardless of chain length.

The SAED <010> zone axis diffraction patterns are rich with details because of the short electron wavelength and the flatness of the Ewald sphere. However, there are numerous unexpected space-group-forbidden reflections observed in the SAED micrographs. For example, 100 is forbidden in space group $P2_1/n$. These were also observed by Allen and

Author Manuscript Author Manuscript Author Manuscript Author Manuscript

coworkers.[23] On examination of individual frames of XFEL data collected down the same axis, these reflections do not appear with any great frequency.

In the structure factors measured by X-ray diffraction, there are few violations of the expected absences for $P2_1/n$ (Figure S7). Furthermore, the refinements of all three structures in $P2_1/n$ proceeded without difficulty; there was no sign of disorder as would be expected if the real symmetry were lower. Therefore, the *n*-glide extinction violations in the SAED patterns are an artifact of the electron diffraction experiment. We note that zone axis diffraction results in many reflections that are near a diffracting condition, which makes dynamical effects from multiple scattering events more likely to produce intensity in spacegroup forbidden reflections. This is why off-zone axis data collection methods are used to collect data for 3D structure determination.[47,48] Ultrathin samples (<10 nm) can be used to avoid dynamical effects from on-axis ED data collection, but for systems like those studied here this would constitute only 2-3 unit cells in the *b* direction and may result in considerable surface effects. We further note that for simulated patterns, an assumption is made that the electron beam is perfectly parallel to the zone axis, while in a real experiment the beam has some divergence, and the sample is not perfectly flat. This can further lead to the presence of forbidden reflections in the experimental data that are not expected from the idealized simulated pattern.[49] Surface reconstructions could additionally contribute, although notably the extra reflections are not observed with such great frequency for the MOChas with an odd number of carbons.

We observe further additional SAED reflections for the even-numbered CX compounds, exemplified in Figures 5f and 5h. We hypothesize that these reflections are explained either by reticular twinning or a *c*-axis lattice doubling model, with simulated patterns for both found in Figure S5. The reflections annotated with white rectangles correspond to the latter model. The two models are mutually exclusive and potentially testable in the future if complete 3D diffraction patterns are collected from C10 or C12. A distinction between the two models is that the twinned case would have alkyl chains oriented differently along roughly a^* and $a^{*\prime}$, whereas the c-axis doubling case all alkyl chains would be oriented along a^*, which is the same direction in both twin components.

The Odd-Even Effect of Interlayer Stacking

Odd-even effects where alkyl chain length impacts packing and order in self-assembling systems have been studied in this and related self-assembling systems.[50] Allen and coworkers showed an odd-even effect of measured layer thicknesses depending on whether the alkyl chain in question has an even number of carbons or an odd number[23] and proposed a role of the terminal methyl group in defining the registry of the layers. However, the models did not predict the antiparallel arrangement of the two layers in the unit cell and therefore predicted the methyl/methyl interface as having opposing angles. The smSFX crystallography models show an alignment of molecules end-to-end across the interface. We contrast the C9 from the C4 and C6 structures for insight into the origin of the packing differences.

The C9 terminal C-C bond is oriented at 40.9° from the inorganic plane, while C4 and C6 are at 31.0 and 32.9 degrees respectively. This modestly steeper angle in the odd-numbered

Author Manuscript Author Manuscript Author Manuscript Author Manuscript

case results in more efficient packing where methyl groups are set into the 4-fold hollow of the next layer. Conversely, in C4 and C6, the methyl groups on one layer are shifted into a 3-fold hollow of the next layer. This difference accounts for the layered thickness deviations observed in the even- and odd- numbered systems.

We also observe differences in registration of the methyl groups from layer to layer at the all-organic interfaces, illustrated in Figure 6. We model the methyl groups as hard spheres having a van der Waals radius of 2.0 Å and accented them in different colors to emphasize the packing arrangements. The two layers are identical and oppositely oriented, but the methyl positions are well-registered between layers in the C9 example. However, in both the C4 and C6, the two layers are not well-registered vertically. Figures 6a and 6b show the complex alignments. AB and CD have uniformity of azimuth and are associated to one another in position by the inorganic phase of the lattice. The termini are colored to show the four distinct registries of the methyl termini within a single unit cell (two complete layers). The relative azimuth is recorded as the colored arrows. On the other hand, the odd-numbered systems are better-registered, despite the alternating azimuthal orientation.

Such subtle stacking effects have been previously shown to play an important role in the crystallization of small-molecule systems without strongly directional intermolecular interactions like hydrogen bonds. For example, Desiraju showed that crystal packing and stacking sequence of a nonhydrogen-bonded material is often governed by the principle of close-packing.[51] This leads to the realization of alternative structures of higher densities in closed packed systems.[52,53] Some works have highlighted how varying peripheral alkyl chain length can dramatically affect the self-assembly behavior of materials.[54] Ultimately, consideration of the space group symmetry into which the alkanethiols crystallize, and understanding the interplay between entropy and geometrical constraints imposed on them helps in understanding the stacking sequence that they adopt.[55]

Conclusions

Atomic resolution smSFX structures provide high-quality structural solutions for compounds whose syntheses yield predominantly small crystals. We obtained a representative sample of silver *n*-alkanethiolates having even and odd numbers of carbon chains with final resolution at the crystallographic standard of 0.833 Å. The C9 sample was further collected to high multiplicity. The C9 excellent redundancy of this dataset may be useful for future method development. It would have been preferable to obtain structures on all samples, especially an additional example having an odd number of carbon units, but such effort will have to be reserved for future experiments. Our results, including the partial indexing results of unsolved examples, are consistent with all members of the series being similar to those complete solutions presented here.

The synthetic direct chalcogenation approach uses exothermic water evolution from the thiol/oxide reaction as part of the driving force to construct the MOChas. The reaction vigor was inversely related to the molecular length. This gives us insight into the limitations of this reaction that can be considered when planning the preparation of more elaborate systems. The microcrystalline products synthesized by this approach are ideal substrates

Author Manuscript Author Manuscript Author Manuscript Author Manuscript

for smSFX experiments because they are air-stable, insoluble, and possess a well-defined surface chemistry.

The inorganic structure and alkyl tilt is highly conserved across the CX family in agreement with earlier work. We find short argentophilic interactions acting between the silver atoms and an alkyl tilt of 22° from the normal of the inorganic plane. The odd-even layer thickness discrepancy is also resolved by demonstrating different packing registries of layers for even-numbered chains (C4 and C6) relative to the odd-numbered chain (C9). Critically the interfacial packing of the layered systems appears sensitive to the orientation of the terminal methyl unit of the alkyl chain. This has important implications for the planning of MOChas having derivatized molecular subunits.

In contrast with most SAMs, the AFM images of MOCha crystals showed largely featureless terraces free of orientational molecular defects and tilt domain boundaries. The interesting twin or sublattice SAED reflections in the even-numbered cases suggest that there may be additional subtle diversity among these compounds, and that there are still several possibilities for domains and disorder in those systems. Care is advised when interpreting SAED measurements of systems like MOCha because of the emergence of intensity in reflections that are normally not observed in X-ray diffraction. Further investigation of the chemistry and geometry of hybrid interfaces is warranted for the future development of more elaborate and functional systems.

Experimental Section

Materials.

Silver (I) oxide (≥ 99%) and *n*-alkanethiols were used as received from Sigma Aldrich. Deionized water (18.2 MΩ·cm) was dispensed from a Millipore direct-Q 8 UV purification system, methanol (≥ 99.8%), ethyl acetate (HPLC grade), and isopropanol (≥ 99%) were obtained from Fisher Scientific, anhydrous tetrahydrofuran (≥99.8%) was obtained from Alfa Aesar, acetone (99.9%) was obtained from Sigma Aldrich and toluene (Baker analyzed ACS reagent) was received from J.T Baker. One-dram vials with polyvinyl lined caps were obtained from Duran Wheaton Kimble. Samples were incubated in a Fisher Scientific Isotemp 500 Series oven and isolated in a Thermo Scientific Sorvall ST 8 Centrifuge.

Synthesis.

Samples were prepared by adding 50 mg of solid Ag_2O and 2-4 equivalents of the liquid thiol to a dram vial. A solvent-free synthesis can be utilized. However, the paste-like consistency of the reaction mixture is inconvenient, and volumetric expansion can cause the product to become impacted. Solvent addition can be used in small amounts to make the reaction easier to mix and handle; typically, 1.5 mL solvent was added to the silver oxide prior to thiol addition. Samples incubate at 75°C in an oven for 72-96 hours. Reactions were typically unstirred. *Safety Notes: Teflon vial closures are recommended to avoid release of vapors under heating. Overheating closures can cause them to seize against the glass creating a breakage hazard. Secondary containment of the samples in a larger sealed jar is advised to avoid a smelly oven.*

Author Manuscript Author Manuscript Author Manuscript Author Manuscript

After incubation, product was isolated via several rounds of centrifugation or settling. The product was stored suspended in isopropanol in a refrigerator. For longer chain samples, longer incubations were sometimes required. We observed that these samples would occasionally undergo a long induction period with apparently no reaction, and then go to completion unexpectedly.

Powder X-ray Diffraction at a lab source and at synchrotron APS 11-BM

Suspensions of product were allowed to dry into powder to perform X-ray diffraction on a Bruker AXS D2 Phaser and at APS 11-BM. Samples were prepared by loading dry powder into a 24.6 × 1.0 mm silicon P type zero diffraction plate and were exposed to a copper Kα radiation source (1.54184 Å) at increments of 0.02°.

High resolution synchrotron powder diffraction data were collected using beamline 11-BM at the Advanced Photon Source (APS), Argonne National Laboratory using an average wavelength of 0.4581 Å. CX Powders were loaded into 0.86 mm diameter Kapton capillary tubes and exposed to the incident beam for 200s. Discrete detectors covering an angular range from −6 to 16° 2θ are scanned over a 34° 2θ range, with data points collected every 0.001° 2θ and scan speed of 0.01°/s.

The 11-BM instrument uses x-ray optics with two platinum-striped mirrors and a double-crystal Si(111) monochromator, where the second crystal has an adjustable sagittal bend.[28] Ion chambers monitor incident flux. A vertical Huber 480 goniometer, equipped with a Heidenhain encoder, positions an analyzer system comprised of twelve perfect Si(111) analyzers and twelve Oxford-Danfysik $LaCl_3$ scintillators, with a spacing of 2° 2θ.[56] Analyzer orientation can be adjusted individually on two axes. A three-axis translation stage holds the sample mounting and allows it to be spun, typically at ~5400 RPM (90 Hz). A Mitsubishi robotic arm is used to mount and dismount samples on the diffractometer.

The diffractometer is controlled via EPICS.[57] Data are collected while continually scanning the diffractometer 2θ arm. A mixture of NIST standard reference materials, Si (SRM 640c) and Al_2O_3 (SRM 676) is used to calibrate the instrument, where the Si lattice constant determines the wavelength for each detector. Corrections are applied for detector sensitivity, 2θ offset, small differences in wavelength between detectors, and the source intensity, as noted by the ion chamber before merging the data into a single set of intensities evenly spaced in 2θ. 2θ positions and d-spacings were gathered by taking the Gaussian regression of the data via Igor Pro software from Wavemetrics Inc.

smSFX at LCLS

Data collection was performed at the CXI endstation at LCLS[39] during experiments designated P216 and LY65. Microcrystals were suspended in compatible carrier solvents and delivered to the XFEL interaction region by the GDVN liquid jet sample delivery system. Aqueous surfactant solution (0.2-0.3% w/v) and water were used as carrier solvents, determined by their suspending power and compatibility with the GDVN. The focusing He gas pressure varied from 300 to 400 psi and the liquid flow rate between 30 to 50 μL/min. Sample concentration varied between 3 mg/mL to 4 mg/mL depending on particle behavior in the suspension. Thaumatin microcrystals were prepared using a standard protocol[58] and

Author Manuscript Author Manuscript Author Manuscript Author Manuscript

delivered to the interaction region as a calibrant for detector panel metrology at LY65. Lysozyme microcrystals were prepared using a standard protocol as a calibrant for P216.

Single-shot diffraction patterns were recorded on a JUNGFRAU 4M detector [59] positioned ~59 mm and ~160 mm from the interaction region to record low resolution reflections. The photon energy of the XFEL pulses was ~18 keV (0.686 Å) at LY65 and 10.5 keV(1.18 Å) at P216. The beam size at the interaction region was ~1 μm using beryllium lens focusing optics. The pulse power and photon energy were characterized by a downstream single-shot spectrometer[60] at LY65. The repetition rate of the XFEL was 120 Hz, delivering 120 pulses per second with a pulse duration of ~30 fs and per-pulse energy of ~1-3 mJ. All data collection was performed in vacuum conditions and under room temperature.

At the high photon energy of the LY65 experiment, the detection efficiency of the downstream spectrometer was low, and the spectrometer background caused significant errors in the measured photon energy. Thus, we implemented a new procedure for background ("pedestal") subtraction for the downstream spectrometer. We averaged several thousand dark shots on the spectrometer and subtracted the result from all subsequent spectra.

smSFX at European XFEL

Data collection was performed at the FXE instrument at the European XFEL.[61,62] Microcrystals were suspended in compatible carrier solvents and delivered to the X-ray interaction region by a GDVN-based liquid jet. The nozzle had a liquid aperture OD of 150 μm and a gas orifice of 100 μm.[63] The focusing He gas pressure varied from 350 to 450 psi (corresponding to a gas flow rate of 20 to 30 mg/min) and the liquid flow rate 100 to 200 μL/min. Suspensions with particle concentrations of 1-2 mg/mL were sonicated for 20 minutes in methanol, the selected carrier solvent, and aliquoted directly into the sample reservoir with no settling time. Because of the 564 kHz intratrain X-ray pulse repetition rate, EuXFEL requires a higher jet velocity than at LCLS in order to refresh sample volume at the interaction region between the arrival of each pulse. For example, with an applied liquid flow rate of 100 µL/min and a Helium flow rate of 30 mg/min, the jet was ~10 µm wide and ~25 m/s fast with a jet length of ~500 µm. The exact intra-train pulse rate was 564 kHz, the 4th subharmonic of 2.25 MHz base repetition rate of EuXFEL machine. The pulses were grouped in trains of 200 pulses with intertrain repetition rate of 10 Hz. We note that methanol is a better carrier solvent for these materials when high speed jets are necessary. The aqueous surfactant solution used at prior experiments is well suited for experiments where jet velocity is not an important parameter. Lysozyme microcrystals were prepared using a standard protocol and delivered to the interaction region as a calibrant for detector panel metrology.[64]

Single-shot diffraction patterns were recorded on the Large Pixel Detector (LPD)[65] positioned ~160 mm and ~500 mm from the interaction region. The photon energy of the XFEL pulses was ~14.9 keV (0.827 Å) and the beam size at the interaction region was ~20 μm full width half max. Each pulse had a duration of 50 fs with a per-pulse energy of ~2.2 mJ at the XFEL source or ~0.7 mJ/pulse at the sample as determined by X-ray gas monitors upstream and downstream from the interaction region, respectively.[66] The X-ray

Author Manuscript Author Manuscript Author Manuscript Author Manuscript

photon energy was constantly monitored by the HIREX single-shot spectrometer installed upstream of the sample.[67] The XFEL photon flux (ca. 10^{12} photons/pulse unattenuated) was attenuated by 10% to 50% depending on detector saturation response. All data collection was performed in atmospheric conditions and under room temperature with the XFEL beam entering an unsealed Kapton chamber.

For the LPD detector at EuXFEL, special care was required to identify and mask “hot pixels” on the detector. We observed that hot pixels often appeared and disappeared on the scale of minutes. Therefore, a separate mask was generated for every individual sub-run (~30 seconds of data or ~60k images). This was accomplished by a preliminary run of the DIALS spotfinder[68] that was used to identify individual pixels producing an unusual number of hits in the spotfinder. A low threshold of 0.1% hit frequency was applied; i.e. any pixel that was detected by the spotfinder in >0.1% of the frames from a sub-run was masked for subsequent processing.

Data Processing

The structure determination follows steps that have been described previously.[20] Briefly, the following steps are required:

The detector internal metrology (relative positions of panels) was refined against a separately collected macromolecular dataset using the methods described in Brewster *et. al*.[69] This step is necessary because the sparse diffraction patterns in smSFX datasets do not yield enough spot coverage to independently refine the positions of individual panels.

For unit cell determination, the DIALS spotfinder was used to harvest diffraction spots from a subset of the full data.[68] Typically 5-10 minutes of data collection is enough for this step. The harvested spots are converted to d-spacings and synthesized into a virtual powder diffraction pattern as described previously.[20] For LPD data collection, these runs were collected at a longer detector distance to improve the sharpness of the powder pattern. For Jungfrau 4M data, because of the smaller pixels and higher X-ray energy, a single detector position with inscribed resolution ~0.8 Å was sufficient for both unit cell determination and structure solution.

When synthesizing virtual powder patterns, we observed that small shifts in the detector position were common over the course of the experiment. This was especially notable at EuXFEL, where the detector position was readjusted manually after every distance change. The quality of powder patterns has a critical dependence on very accurate (~5-10 um) calibration of the beam center. Therefore, the beam center was adjusted as an integral part of the powder pattern creation. We identified a single isolated peak in the diffraction pattern and computed its width as a standard deviation of all individual observations of that peak. We then performed a grid search in decreasing steps (typically from 2 pixels to 1/32 pixel) until the peak sharpness was optimized.

After a properly calibrated virtual powder diffraction pattern was prepared, we manually selected 20-25 d-spacings from the pattern to use for unit cell determination. We obtained the most consistent results using the commercial crystallography program TOPAS-

Author Manuscript Author Manuscript Author Manuscript Author Manuscript

Academic.[70] Often this resulted in several reasonable unit cell proposals. For the closely related series of unit cells described here, it was trivial to identify the matching cell, but for a fully unknown sample it is often helpful to attempt *cctbx.small_cell* indexing of a subset of the data with several unit cell candidates. The cell with the highest indexing rate is typically the correct one.

After TOPAS unit cell determination, we proceeded with *cctbx.small_cell* indexing and integration as previously described. In the *cctbx.xfel.merge* scaling and merging step, we implemented a new weighting scheme for scaling individual frames, where the uncertainties on individual observations are assigned as $1/(I_{calc}^2+\sigma(I_o)^2)$ with $\sigma(I_o)$ representing the uncertainty on the measured net counts in a diffraction peak. This new weighting scheme is activated by setting scaling.weights=icalc_sigma as a parameter for *cctbx.xfel.merge*. We note this weighting scheme is similar to the one used for refinement in ShelXL, where the weight of an observation is typically $1/(\sigma(I_o)^2 + (ap)^2+bp)$ with $p = 1/3\ I_o^2 + 2/3\ I_c^2$ and a, b small, user-defined parameters. Our weighting scheme for scaling is a simplified approach where I_o is not considered, a is unity and b is zero.

After merging, the ~0.8 Å resolution datasets were solved using ShelXT with the default settings. Refinement proceeded routinely using ShelXL. We refined an extinction parameter for all structures (ShelXL instruction EXTI), which is an empirical model for attenuation of the strongest structure factors. While we do not believe that literal crystallographic extinction is possible in serial microcrystal diffraction, the refinements with extinction resulted in more interpretable difference maps, so we argue that this technique is beneficial. At the end of the refinement process, we repeated the scaling and merging step with the working model (with isotropic displacement parameters) as a scaling reference as described previously. In the final refinements, hydrogen atoms were placed in calculated positions with riding isotropic displacement parameters; all other atoms were refined with unrestrained anisotropic displacement parameters.[41]

Scanning Electron Microscopy

SEM images were collected on a Phenom Pro X, with accelerating voltages of 5 keV to 15 keV. Samples were prepared by creating a dilute suspension of the product in isopropanol and adding 1-2 drops of this suspension directly onto the specimen holder, a glass substrate, or a PELCO tab adhesive.

Transmission Electron Microscopy

TEM samples were prepared by drop-casting a 4.0 μL droplet of a concentrated isopropanol solution containing a dispersion of preformed MOCHA microparticles onto the surface of a lacey-Carbon TEM-grid (Ted Pella, Inc., Redding, CA). The applied droplet was allowed to completely air-dry on the grid, and then stored briefly in dark, ambient conditions until being used. Characterization was performed on UConn ThermoFisher (Waltham, MA) Talos TEM operating at 300 keV with a beam current of 0.277 nA and a dose rate of 0.06 $e^-/Å^2s$**.** Diffraction patterns and d-spacing measurements were acquired using a 200 μm selected area diffraction (SAD) aperture using ThermoFisher TIA software. Further specification for instrument settings can be found in the supporting information.

Author Manuscript Author Manuscript Author Manuscript Author Manuscript

Atomic Force Microscopy

Surface topography was measured using a Cypher ES Environmental AFM (Asylum Research) and an OMCL-C160TS probe (Olympus) in AC mode. Regions with 1×1 μm^2 dimensions were studied to observe crystal step geometries for individual and multiple layers of the various C-length specimens. Based on representative topographic images for each condition considered, the heights of individual crystal layers were extracted from single and multiple stacked crystal layers.

Supplementary Material

Refer to Web version on PubMed Central for supplementary material.

Acknowledgements:

The authors are grateful to the EuXFEL and LCLS technical and user support staff for their invaluable contribution to this effort, including Chris Kupitz and Vasilii Bazhenov. Norberto Masciocchi is acknowledged for helpful discussions regarding powder indexing in TOPAS. JNH, ASB, EAS, DWP, DM, VO, PK and MA were supported by the US Department of Energy Integrated Computational and Data Infrastructure for Scientific Discovery grant DE-SC0022215. EAS was supported by the Department of Energy and National Nuclear Security Administration Stewardship Science Graduate Fellowship. Research was supported by the NIH grant GM117126 to NKS. JPB and NKS were supported by the Exascale Computing Project (grant 17-SC-20-SC), a collaborative effort of the Department of Energy (DOE) Office of Science and the National Nuclear Security Administration. WL and BDH were supported by the University of Connecticut Institute of Materials Science. Use of the Linac Coherent Light Source (LCLS), SLAC National Accelerator Laboratory, is supported by the U.S. Department of Energy, Office of Science, Office of Basic Energy Sciences under Contract No. DE-AC02-76SF00515. This research used resources of the National Energy Research Scientific Computing Center (NERSC), a U.S. Department of Energy Office of Science User Facility located at Lawrence Berkeley National Laboratory, operated under Contract No. DE-AC02-05CH11231. Use of the Advanced Photon Source at Argonne National Laboratory was supported by the U. S. Department of Energy, Office of Science, Office of Basic Energy Sciences, under Contract No. DE-AC02-06CH11357. We acknowledge European XFEL in Schenefeld, Germany, for provision of X-ray free-electron laser beamtime at Scientific Instrument FXE (Femtosecond X-Ray Experiments).

Data and materials availability:

Code for generating powder patterns and interfacing with GSAS-II was implemented in a DIALS/CCTBX environment, currently available from https://github.com/cctbx/cctbx-project.

Crystallographic data for SFX collected C4, C6, C9 structures are available free of charge via the Cambridge Crystallographic Data Centre (CCDC) with deposition numbers 2245271, 2245272, and 2245273, respectively. Raw XFEL SFX data for experiment LY65 are available free of charge via the Coherent X-ray Imaging Database (CXIDB), accession number 214, https://www.cxidb.org/id-214.html.

References

1. Sandhyarani N; Pradeep T, An Investigation of the Structure and Properties of Layered Copper Thiolates. J. Mater. Chem 2001, 11, 1294–1299. 10.1039/B009837J
2. Cha S-H; Kim J-U; Kim K-H; Lee J-C, Preparation and Photoluminescent Properties of Gold(I)–Alkanethiolate Complexes Having Highly Ordered Supramolecular Structures. Chem. Mater 2007, 19, 6297–6303. 10.1021/cm7024944

Author Manuscript Author Manuscript Author Manuscript Author Manuscript

3. Lavenn C; Guillou N; Monge M; Podbevšek D; Ledoux G; Fateeva A; Demessence A, Shedding Light on an Ultra-Bright Photoluminescent Lamellar Gold Thiolate Coordination Polymer [Au(P-SPhCO$_2$Me)]N. Chem. Commun 2016, 52, 9063–9066. 10.1039/C5CC10448C
4. Yan H; Hohman JN; Li FH; Jia C; Solis-Ibarra D; Wu B; Dahl JEP; Carlson RMK; Tkachenko BA; Fokin AA; Schreiner PR; Vailionis A; Kim TR; Devereaux TP; Shen Z-X; Melosh NA, Hybrid Metal–Organic Chalcogenide Nanowires with Electrically Conductive Inorganic Core through Diamondoid-Directed Assembly. Nat. Mater 2017, 16, 349–355. 10.1038/nmat4823 [PubMed: 28024157]
5. Schriber EA; Popple DC; Yeung M; Brady MA; Corlett SA; Hohman JN, Mithrene Is a Self-Assembling Robustly Blue Luminescent Metal–Organic Chalcogenolate Assembly for 2D Optoelectronic Applications. ACS Appl. Nano Mater 2018, 1, 3498–3508. 10.1021/acsanm.8b00662
6. Scarano D; Cesano F, Graphene and Other 2d Layered Nanomaterials and Hybrid Structures: Synthesis, Properties and Applications. Materials 2021, 14, 7108. [PubMed: 34885263]
7. Paritmongkol W; Sakurada T; Lee WS; Wan R; Müller P; Tisdale WA, Size and Quality Enhancement of 2d Semiconducting Metal–Organic Chalcogenolates by Amine Addition. J. Am. Chem. Soc 2021, 143, 20256–20263. 10.1021/jacs.1c09106 [PubMed: 34806381]
8. Wang G-E; Luo S; Di T; Fu Z; Xu G, Layered Organic Metal Chalcogenides (Omcs): From Bulk to Two-Dimensional Materials. Angew. Chem., Int. Ed 2022, 61, e202203151. 10.1002/anie.202203151
9. Mills HA; Jones CG; Anderson KP; Ready AD; Djurovich PI; Khan SI; Hohman JN; Nelson HM; Spokoyny AM, Sterically Invariant Carborane-Based Ligands for the Morphological and Electronic Control of Metal–Organic Chalcogenolate Assemblies. Chem. Mater 2022, 34, 6933–6943. 10.1021/acs.chemmater.2c01319
10. Sakurada T; Cho Y; Paritmongkol W; Lee WS; Wan R; Su A; Shcherbakov-Wu W; Müller P; Kulik HJ; Tisdale WA, 1D Hybrid Semiconductor Silver 2,6-Difluorophenylselenolate. J. Am. Chem. Soc 2023, 145, 5183–5190. 10.1021/jacs.2c11896 [PubMed: 36811999]
11. Rabl H; Myakala SN; Rath J; Fickl B; Schubert JS; Apaydin DH; Eder D, Microwave-Assisted Synthesis of Metal-Organic Chalcogenolate Assemblies as Electrocatalysts for Syngas Production. Communications Chemistry 2023, 6, 43. 10.1038/s42004-023-00843-3 [PubMed: 36859623]
12. Bensebaa F; Voicu R; Huron L; Ellis TH; Kruus E, Kinetics of Formation of Long-Chain N-Alkanethiolate Monolayers on Polycrystalline Gold. Langmuir 1997, 13, 5335–5340.
13. Bensebaa F; Ellis TH; Kruus E; Voicu R; Zhou Y, Characterization of Self-Assembled Bilayers: Silver–Alkanethiolates. Langmuir 1998, 14, 6579–6587. 10.1021/la980718g
14. Parikh AN; Gillmor SD; Beers JD; Beardmore KM; Cutts RW; Swanson BI, Characterization of Chain Molecular Assemblies in Long-Chain, Layered Silver Thiolates: A Joint Infrared Spectroscopy and X-Ray Diffraction Study. The Journal of Physical Chemistry B 1999, 103, 2850–2861. 10.1021/jp983938b
15. Bardeau JF; Parikh AN; Beers JD; Swanson BI, Phase Behavior of a Structurally Constrained Organic-Inorganic Crystal: Temperature-Dependent Infrared Spectroscopy of Silver N-Dodecanethiolate. J. Phys. Chem. B 2000, 104, 627–635. 10.1021/jp992156v
16. Levchenko AA; Yee CK; Parikh AN; Navrotsky A, Energetics of Self-Assembly and Chain Confinement in Silver Alkanethiolates: Enthalpy-Entropy Interplay. Chem. Mater 2005, 17, 5428–5438. 10.1021/cm050961i
17. Han P; Kurland AR; Giordano AN; Nanayakkara SU; Blake MM; Pochas CM; Weiss PS, Heads and Tails: Simultaneous Exposed and Buried Interface Imaging of Monolayers. ACS Nano 2009, 3, 3115–3121. 10.1021/nn901030x [PubMed: 19772297]
18. Jung JS; Ko SJ; Lee HB; Lee SB; Kim HJ; Oh JM, Hierarchical Ag Nanostructures Fabricated from Silver Coordination Polymers for Antibacterial Surface. Polymers (Basel) 2019, 11. 10.3390/polym11010155
19. Schmidbaur H; Schier A, Argentophilic Interactions. Angew. Chem., Int. Ed 2015, 54, 746–784. 10.1002/anie.201405936
20. Schriber EA; Paley DW; Bolotovsky R; Rosenberg DJ; Sierra RG; Aquila A; Mendez D; Poitevin F; Blaschke JP; Bhowmick A; Kelly RP; Hunter M; Hayes B; Popple DC; Yeung M; Pareja-Rivera

Author Manuscript Author Manuscript Author Manuscript Author Manuscript

C; Lisova S; Tono K; Sugahara M; Owada S; Kuykendall T; Yao K; Schuck PJ; Solis-Ibarra D; Sauter NK; Brewster AS; Hohman JN, Chemical Crystallography by Serial Femtosecond X-Ray Diffraction. Nature 2022, 601, 360–365. 10.1038/s41586-021-04218-3 [PubMed: 35046599]

21. Dance IG; Fisher KJ; Banda RMH; Scudder ML, Layered Structure of Crystalline Compounds Silver Thiolates (AgSR). Inorg. Chem 1991, 30, 183–187. 10.1021/ic00002a008
22. de la Rama LP; Hu L; Ye Z; Efremov MY; Allen LH, Size Effect and Odd–Even Alternation in the Melting of Single and Stacked AgSCN Layers: Synthesis and Nanocalorimetry Measurements. J. Am. Chem. Soc 2013, 135, 14286–14298. 10.1021/ja4059958 [PubMed: 23977984]
23. Ye Z; Rama L. P. d. l.; Y. Efremov M; Zuo J-M; H. Allen L, Approaching the Size Limit of Organometallic Layers: Synthesis and Characterization of Highly Ordered Silver–Thiolate Lamellae with Ultra-Short Chain Lengths. Dalton Trans. 2016, 45, 18954–18966. 10.1039/C6DT03629E [PubMed: 27844087]
24. Ning H; Zeng Y; Zuo S; Kershaw SV; Hou Y; Li Y; Li X; Zhang J; Yi Y; Jing L; Li J; Gao M, Two-Dimensional and Subnanometer-Thin Quasi-Copper-Sulfide Semiconductor Formed Upon Copper–Copper Bonding. ACS Nano 2021, 15, 873–883. 10.1021/acsnano.0c07388 [PubMed: 33404214]
25. Fijolek HG; Grohal JR; Sample JL; Natan MJ, A Facile Trans to Gauche Conversion in Layered Silver Butanethiolate. Inorg. Chem 1997, 36, 622–628. 10.1021/ic961268n
26. Trang B; Yeung M; Popple DC; Schriber EA; Brady MA; Kuykendall TR; Hohman JN, Tarnishing Silver Metal into Mithrene. J. Am. Chem. Soc 2018, 140, 13892–13903. 10.1021/jacs.8b08878 [PubMed: 30265001]
27. Joback KG; Reid RC, Estimation of Pure-Component Properties from Group-Contributions. Chem. Eng. Commun 1987, 57, 233–243. 10.1080/00986448708960487
28. Wang J; Toby BH; Lee PL; Ribaud L; Antao SM; Kurtz C; Ramanathan M; Von Dreele RB; Beno MA, A Dedicated Powder Diffraction Beamline at the Advanced Photon Source: Commissioning and Early Operational Results. Rev. Sci. Instrum 2008, 79, 085105. 10.1063/1.2969260 [PubMed: 19044378]
29. Vanoppen P; Grim PCM; Rücker M; De Feyter S; Moessner G; Valiyaveettil S; Müllen K; De Schryver FC, Solvent Codeposition and Cis–Trans Isomerization of Isophthalic Acid Derivatives Studied by Stm. J. Phys. Chem 1996, 100, 19636–19641. 10.1021/jp962737+
30. Tao F; Bernasek SL, Self-Assembly of 5-Octadecyloxyisophthalic Acid and Its Coadsorption with Terephthalic Acid. Surf. Sci 2007, 601, 2284–2290. 10.1016/j.susc.2007.03.037
31. Bang JJ; Rupp KK; Russell SR; Choong SW; Claridge SA, Sitting Phases of Polymerizable Amphiphiles for Controlled Functionalization of Layered Materials. J. Am. Chem. Soc 2016, 138, 4448–4457. 10.1021/jacs.5b13179 [PubMed: 26974686]
32. Love JC; Estroff LA; Kriebel JK; Nuzzo RG; Whitesides GM, Self-Assembled Monolayers of Thiolates on Metals as a Form of Nanotechnology. Chem. Rev 2005, 105, 1103–1169. 10.1021/cr0300789 [PubMed: 15826011]
33. Fenter P; Eisenberger P; Li J; Camillone N; Bernasek S; Scoles G; Ramanarayanan TA; Liang KS, Structure of Octadecyl Thiol Self-Assembled on the Silver(111) Surface: An Incommensurate Monolayer. Langmuir 1991, 7, 2013–2016. 10.1021/la00058a008
34. Ulman A; Eilers JE; Tillman N, Packing and Molecular-Orientation of Alkanethiol Monolayers on Gold Surfaces. Langmuir 1989, 5, 1147–1152.
35. Camillone N; Eisenberger P; Leung TYB; Schwartz P; Scoles G; Poirier GE; Tarlov MJ, New Monolayer Phases of *n*-Alkane Thiols Self-Assembled on Au(111) - Preparation, Surface Characterization, and Imaging. J. Chem. Phys 1994, 101, 11031–11036.
36. Weiss PS, Functional Molecules and Assemblies in Controlled Environments: Formation and Measurements. Acc. Chem. Res 2008, 41, 1772–1781. 10.1021/ar8001443 [PubMed: 18847229]
37. Fuchs DJ; Weiss PS, Insertion of 1,10-Decanedithiol in Decanethiolate Self-Assembled Monolayers on Au{111}. Nanotechnology 2007, 18, 044021. 044021 10.1088/0957-4484/18/4/044021
38. Boutet S; Lomb L; Williams GJ; Barends TR; Aquila A; Doak RB; Weierstall U; DePonte DP; Steinbrener J; Shoeman RL; Messerschmidt M; Barty A; White TA; Kassemeyer S; Kirian RA; Seibert MM; Montanez PA; Kenney C; Herbst R; Hart P; Pines J; Haller G; Gruner SM; Philipp

Author Manuscript Author Manuscript Author Manuscript Author Manuscript

HT; Tate MW; Hromalik M; Koerner LJ; van Bakel N; Morse J; Ghonsalves W; Arnlund D; Bogan MJ; Caleman C; Fromme R; Hampton CY; Hunter MS; Johansson LC; Katona G; Kupitz C; Liang M; Martin AV; Nass K; Redecke L; Stellato F; Timneanu N; Wang D; Zatsepin NA; Schafer D; Defever J; Neutze R; Fromme P; Spence JC; Chapman HN; Schlichting I, High-Resolution Protein Structure Determination by Serial Femtosecond Crystallography. Science 2012, 337, 362–4. 10.1126/science.1217737 [PubMed: 22653729]

39. Liang M; Williams GJ; Messerschmidt M; Seibert MM; Montanez PA; Hayes M; Milathianaki D; Aquila A; Hunter MS; Koglin JE; Schafer DW; Guillet S; Busse A; Bergan R; Olson W; Fox K; Stewart N; Curtis R; Miahnahri AA; Boutet S, The Coherent X-Ray Imaging Instrument at the Linac Coherent Light Source. J. Synchrotron Radiat 2015, 22, 514–519. 10.1107/S160057751500449X [PubMed: 25931062]
40. Decking W; Abeghyan S; Abramian P; Abramsky A; Aguirre A; Albrecht C; Alou P; Altarelli M; Altmann P; Amyan K; Anashin V; Apostolov E; Appel K; Auguste D; Ayvazyan V; Baark S; Babies F; Baboi N; Bak P; Balandin V; Baldinger R; Baranasic B; Barbanotti S; Belikov O; Belokurov V; Belova L; Belyakov V; Berry S; Bertucci M; Beutner B; Block A; Blöcher M; Böckmann T; Bohm C; Böhnert M; Bondar V; Bondarchuk E; Bonezzi M; Borowiec P; Bösch C; Bösenberg U; Bosotti A; Böspflug R; Bousonville M; Boyd E; Bozhko Y; Brand A; Branlard J; Briechle S; Brinker F; Brinker S; Brinkmann R; Brockhauser S; Brovko O; Brück H; Brüdgam A; Butkowski L; Büttner T; Calero J; Castro-Carballo E; Cattalanotto G; Charrier J; Chen J; Cherepenko A; Cheskidov V; Chiodini M; Chong A; Choroba S; Chorowski M; Churanov D; Cichalewski W; Clausen M; Clement W; Cloué C; Cobos JA; Coppola N; Cunis S; Czuba K; Czwalinna M; D'Almagne B; Dammann J; Danared H; de Zubiaurre Wagner A; Delfs A; Delfs T; Dietrich F; Dietrich T; Dohlus M; Dommach M; Donat A; Dong X; Doynikov N; Dressel M; Duda M; Duda P; Eckoldt H; Ehsan W; Eidam J; Eints F; Engling C; Englisch U; Ermakov A; Escherich K; Eschke J; Saldin E; Faesing M; Fallou A; Felber M; Fenner M; Fernandes B; Fernández JM; Feuker S; Filippakopoulos K; Floettmann K; Fogel V; Fontaine M; Francés A; Martin IF; Freund W; Freyermuth T; Friedland M; Fröhlich L; Fusetti M; Fydrych J; Gallas A; García O; Garcia-Tabares L; Geloni G; Gerasimova N; Gerth C; Geßler P; Gharibyan V; Gloor M; Głowinkowski J; Goessel A; Gołębiewski Z; Golubeva N; Grabowski W; Graeff W; Grebentsov A; Grecki M; Grevsmuehl T; Gross M; Grosse-Wortmann U; Grünert J; Grunewald S; Grzegory P; Feng G; Guler H; Gusev G; Gutierrez JL; Hagge L; Hamberg M; Hanneken R; Harms E; Hartl I; Hauberg A; Hauf S; Hauschildt J; Hauser J; Havlicek J; Hedqvist A; Heidbrook N; Hellberg F; Henning D; Hensler O; Hermann T; Hidvégi A; Hierholzer M; Hintz H; Hoffmann F; Hoffmann M; Hoffmann M; Holler Y; Hüning M; Ignatenko A; Ilchen M; Iluk A; Iversen J; Iversen J; Izquierdo M; Jachmann L; Jardon N; Jastrow U; Jensch K; Jensen J; Jeżabek M; Jidda M; Jin H; Johansson N; Jonas R; Kaabi W; Kaefer D; Kammering R; Kapitza H; Karabekyan S; Karstensen S; Kasprzak K; Katalev V; Keese D; Keil B; Kholopov M; Killenberger M; Kitaev B; Klimchenko Y; Klos R; Knebel L; Koch A; Koepke M; Köhler S; Köhler W; Kohlstrunk N; Konopkova Z; Konstantinov A; Kook W; Koprek W; Körfer M; Korth O; Kosarev A; Kosiński K; Kostin D; Kot Y; Kotarba A; Kozak T; Kozak V; Kramert R; Krasilnikov M; Krasnov A; Krause B; Kravchuk L; Krebs O; Kretschmer R; Kreutzkamp J; Kröplin O; Krzysik K; Kube G; Kuehn H; Kujala N; Kulikov V; Kuzminych V; La Civita D; Lacroix M; Lamb T; Lancetov A; Larsson M; Le Pinvidic D; Lederer S; Lensch T; Lenz D; Leuschner A; Levenhagen F; Li Y; Liebing J; Lilje L; Limberg T; Lipka D; List B; Liu J; Liu S; Lorbeer B; Lorkiewicz J; Lu HH; Ludwig F; Machau K; Maciocha W; Madec C; Magueur C; Maiano C; Maksimova I; Malcher K; Maltezopoulos T; Mamoshkina E; Manschwetus B; Marcellini F; Marinkovic G; Martinez T; Martirosyan H; Maschmann W; Maslov M; Matheisen A; Mavric U; Meißner J; Meissner K; Messerschmidt M; Meyners N; Michalski G; Michelato P; Mildner N; Moe M; Moglia F; Mohr C; Mohr S; Möller W; Mommerz M; Monaco L; Montiel C; Moretti M; Morozov I; Morozov P; Mross D, A Mhz-Repetition-Rate Hard X-Ray Free-Electron Laser Driven by a Superconducting Linear Accelerator. Nat. Photonics 2020, 14, 391–397. 10.1038/s41566-020-0607-z
41. DePonte DP; Weierstall U; Schmidt K; Warner J; Starodub D; Spence JCH; Doak RB, Gas Dynamic Virtual Nozzle for Generation of Microscopic Droplet Streams. J. Phys. D: Appl. Phys 2008, 41, 195505. 10.1088/0022-3727/41/19/195505
42. Knoška J; Adriano L; Awel S; Beyerlein KR; Yefanov O; Oberthuer D; Peña Murillo GE; Roth N; Sarrou I; Villanueva-Perez P; Wiedorn MO; Wilde F; Bajt S; Chapman HN; Heymann M,

Author Manuscript Author Manuscript Author Manuscript Author Manuscript

Ultracompact 3D Microfluidics for Time-Resolved Structural Biology. Nat. Commun 2020, 11, 657. 10.1038/s41467-020-14434-6 [PubMed: 32005876]

43. Steller I; Bolotovsky R; Rossmann MG, An Algorithm for Automatic Indexing of Oscillation Images Using Fourier Analysis. J. Appl. Cryst 1997, 30, 1036–1040.
44. Sauter NK; Grosse-Kunstleve RW; Adams PD, Robust Indexing for Automatic Data Collection. J. Appl. Crystallogr 2004, 37, 399–409. [PubMed: 20090869]
45. Brewster AS; Sawaya MR; Rodriguez J; Hattne J; Echols N; McFarlane HT; Cascio D; Adams PD; Eisenberg DS; Sauter NK, Indexing Amyloid Peptide Diffraction from Serial Femtosecond Crystallography: New Algorithms for Sparse Patterns. Acta Crystallogr D Biol Crystallogr 2015, 71, 357–66. 10.1107/S1399004714026145 [PubMed: 25664747]
46. Wells AF, Structural Inorganic Chemistry. 5th ed.; Oxford University Press: Oxford, 1984.
47. Zhang D; Oleynikov P; Hovmöller S; Zou X, Collecting 3d Electron Diffraction Data by the Rotation Method. Z. Kristallogr 2010, 225, 94–102. 10.1524/zkri.2010.1202
48. Gemmi M; Lanza AE, 3d Electron Diffraction Techniques. Acta Crystallographica Section B 2019, 75, 495–504. doi:10.1107/S2052520619007510
49. Nagakura S; Nakamura Y; Suzuki T, Forbidden Reflection Intensity in Electron Diffraction and Its Influence on the Crystal Structure Image. Japanese Journal of Applied Physics 1982, 21, L449. 10.1143/JJAP.21.L449
50. Tao F; Bernasek SL, Understanding Odd–Even Effects in Organic Self-Assembled Monolayers. Chem. Rev 2007, 107, 1408–1453. 10.1021/cr050258d [PubMed: 17439290]
51. Desiraju GR, Crystal Engineering: From Molecule to Crystal. J. Am. Chem. Soc 2013, 135, 9952–9967. 10.1021/ja403264c [PubMed: 23750552]
52. Brock CP; Dunitz JD, Towards a Grammar of Crystal Packing. Chem. Mater 1994, 6, 1118–1127. 10.1021/cm00044a010
53. Cersonsky RK; van Anders G; Dodd PM; Glotzer SC, Relevance of Packing to Colloidal Self-Assembly. Proc. Natl. Acad. Sci. U. S. A 2018, 115, 1439–1444. 10.1073/pnas.1720139115 [PubMed: 29382766]
54. Herkert L; Selter P; Daniliuc CG; Bäumer N; Palakkal JP; Fernández G; Hansen MR, Tuning the Molecular Packing of Self-Assembled Amphiphilic Ptii Complexes by Varying the Hydrophilic Side-Chain Length. Chem. Eur. J 2021, 27, 4617–4626. 10.1002/chem.202003445 [PubMed: 33350532]
55. Manoharan VN, Colloidal Matter: Packing, Geometry, and Entropy. Science 2015, 349, 1253751. 10.1126/science.1253751; 15 10.1126/science.1253751 [PubMed: 26315444]
56. Lee PL; Shu D; Ramanathan M; Preissner C; Wang J; Beno MA; Von Dreele RB; Ribaud L; Kurtz C; Antao SM; Jiao X; Toby BH, A Twelve-Analyzer Detector System for High-Resolution Powder Diffraction. J. Synchrotron Radiat 2008, 15, 427–432. doi:10.1107/S0909049508018438 [PubMed: 18728312]
57. Dalesio LR; Hill JO; Kraimer M; Lewis S; Murray D; Hunt S; Watson W; Clausen M; Dalesio J, The Experimental Physics and Industrial Control System Architecture: Past, Present, and Future. Nuclear Instruments and Methods in Physics Research Section A: Accelerators, Spectrometers, Detectors and Associated Equipment 1994, 352, 179–184. 10.1016/0168-9002(94)91493-1
58. Nass K; Meinhart A; Barends TRM; Foucar L; Gorel A; Aquila A; Botha S; Doak RB; Koglin J; Liang M; Shoeman RL; Williams G; Boutet S; Schlichting I, Protein Structure Determination by Single-Wavelength Anomalous Diffraction Phasing of X-Ray Free-Electron Laser Data. IUCrJ 2016, 3, 180–191. 10.1107/S2052252516002980
59. Leonarski F; Redford S; Mozzanica A; Lopez-Cuenca C; Panepucci E; Nass K; Ozerov D; Vera L; Olieric V; Buntschu D; Schneider R; Tinti G; Froejdh E; Diederichs K; Bunk O; Schmitt B; Wang M, Fast and Accurate Data Collection for Macromolecular Crystallography Using the Jungfrau Detector. Nat. Methods 2018, 15, 799–804. 10.1038/s41592-018-0143-7 [PubMed: 30275593]
60. Zhu D; Cammarata M; Feldkamp JM; Fritz DM; Hastings JB; Lee S; Lemke HT; Robert A; Turner JL; Feng Y, A Single-Shot Transmissive Spectrometer for Hard X-Ray Free Electron Lasers. Appl. Phys. Lett 2012, 101, 034103. 10.1063/1.4736725
61. Galler A; Gawelda W; Biednov M; Bomer C; Britz A; Brockhauser S; Choi TK; Diez M; Frankenberger P; French M; Görries D; Hart M; Hauf S; Khakhulin D; Knoll M; Korsch T;

Author Manuscript Author Manuscript Author Manuscript Author Manuscript

Kubicek K; Kuster M; Lang P; Alves Lima F; Otte F; Schulz S; Zalden P; Bressler C, Scientific Instrument Femtosecond X-Ray Experiments (FXE): Instrumentation and Baseline Experimental Capabilities. J. Synchrotron Radiat 2019, 26, 1432–1447. 10.1107/S1600577519006647 [PubMed: 31490131]

62. Khakhulin D; Otte F; Biednov M; Bömer C; Choi T-K; Diez M; Galler A; Jiang Y; Kubicek K; Lima FA; Rodriguez-Fernandez A; Zalden P; Gawelda W; Bressler C, Ultrafast X-Ray Photochemistry at European XFEL: Capabilities of the Femtosecond X-Ray Experiments (FXE) Instrument. Applied Sciences 2020, 10, 995. 10.3390/app10030995
63. Vakili M; Bielecki J; Knoška J; Otte F; Han H; Kloos M; Schubert R; Delmas E; Mills G; de Wijn R; Letrun R; Dold S; Bean R; Round A; Kim Y; Lima FA; Dörner K; Valerio J; Heymann M; Mancuso AP; Schulz J, 3d Printed Devices and Infrastructure for Liquid Sample Delivery at the European XFEL. J. Synchrotron Radiat 2022, 29, 331–346. 10.1107/S1600577521013370 [PubMed: 35254295]
64. Kirkwood HJ; de Wijn R; Mills G; Letrun R; Kloos M; Vakili M; Karnevskiy M; Ahmed K; Bean RJ; Bielecki J; Dall'Antonia F; Kim Y; Kim C; Koliyadu J; Round A; Sato T; Sikorski M; Vagovič P; Sztuk-Dambietz J; Mancuso AP, A Multi-Million Image Serial Femtosecond Crystallography Dataset Collected at the European XFEL. Scientific Data 2022, 9, 161. 10.1038/s41597-022-01266-w [PubMed: 35414146]
65. Hart M; Angelsen C; Burge S; Coughlan J; Halsall R; Koch A; Kuster M; Nicholls T; Prydderch M; Seller P; Thomas S; Blue A; Joy A; O'Shea V; Wing M In Development of the Lpd, a High Dynamic Range Pixel Detector for the European XFEL, 2012 IEEE Nuclear Science Symposium and Medical Imaging Conference Record (NSS/MIC), 2012/10//; 2012; pp 534–537.
66. Coelho A, TOPAS and TOPAS-Academic: An Optimization Program Integrating Computer Algebra and Crystallographic Objects Written in C++. J. Appl. Crystallogr 2018, 51, 210–218. doi:10.1107/S1600576718000183
67. Kujala N; Freund W; Liu J; Koch A; Falk T; Planas M; Dietrich F; Laksman J; Maltezopoulos T; Risch J; Dall'Antonia F; Grünert J, Hard X-Ray Single-Shot Spectrometer at the European X-Ray Free-Electron Laser. Rev. Sci. Instrum 2020, 91, 103101. 10.1063/5.0019935 [PubMed: 33138553]
68. Winter G; Waterman DG; Parkhurst JM; Brewster AS; Gildea RJ; Gerstel M; Fuentes-Montero L; Vollmar M; Michels-Clark T; Young ID; Sauter NK; Evans G, Dials: Implementation and Evaluation of a New Integration Package. Acta Crystallogr D Struct Biol 2018, 74, 85–97. 10.1107/s2059798317017235 [PubMed: 29533234]
69. Brewster AS; Waterman DG; Parkhurst JM; Gildea RJ; Young ID; O'Riordan LJ; Yano J; Winter G; Evans G; Sauter NK, Improving Signal Strength in Serial Crystallography with Dials Geometry Refinement. Acta Crystallographica Section D 2018, 74, 877–894. doi:10.1107/S2059798318009191
70. Perl J; Shin J; Schumann J; Faddegon B; Paganetti H, Topas: An Innovative Proton Monte Carlo Platform for Research and Clinical Applications. Med Phys 2012, 39, 6818–37. 10.1118/1.4758060 [PubMed: 23127075]

Author Manuscript Author Manuscript Author Manuscript Author Manuscript

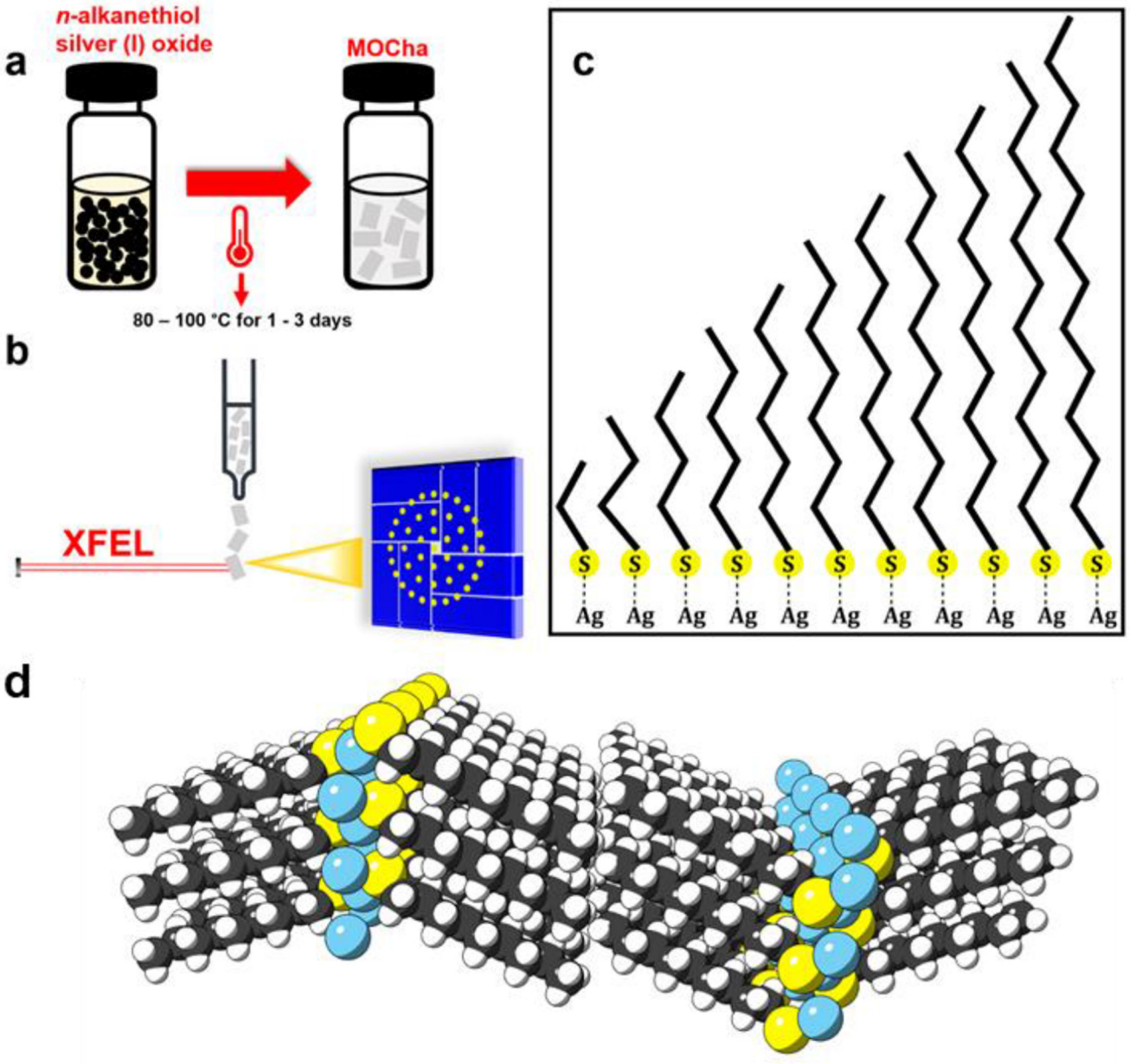

Figure 1:

a) Illustration of the synthetic approach used to prepare alkanethiolates. b) Schematic of smSFX experiment showing how randomly oriented microcrystals interact with the XFEL pulse for the collection of partial diffraction frames recorded on the detector (blue). (c) Alkyl chain lengths studied range from two (2) to twelve (12). d) A space-filling perspective model of the C9 crystal structure depicting the general organization of the silver *n*-alkanethiolates. The silver atoms (blue) are in a nominally 2D layer, coordinated by the sulfur atoms. Note that alkyl chains are packed end-to-end.

Author Manuscript Author Manuscript Author Manuscript Author Manuscript

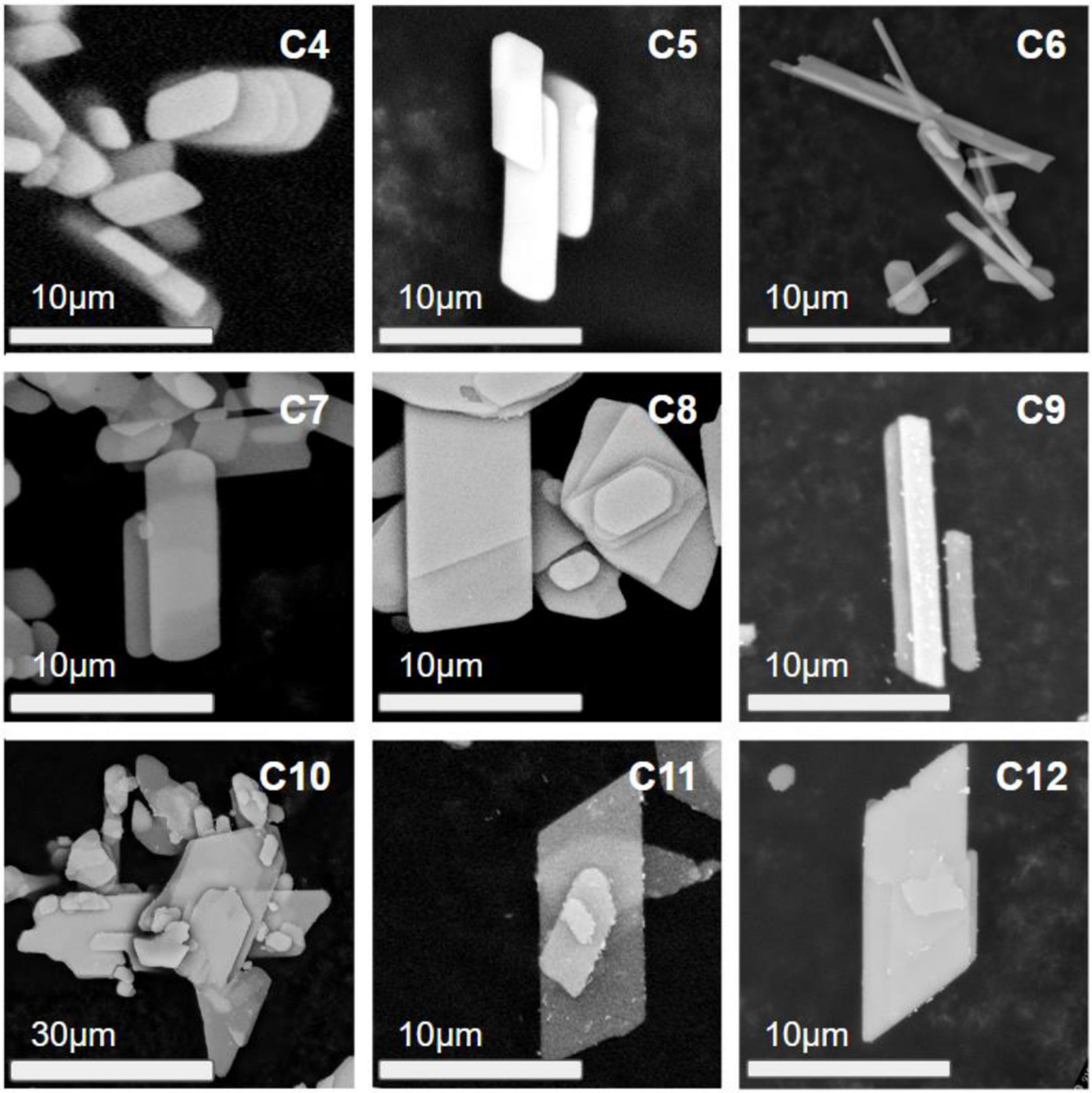

Figure 2:
Example morphologies of the various silver *n*-alkanethiolates over the range of chain length 4-12. For this work, C2, C3, and C12 morphologies proved a poor match for smSFX characterization because of a lack of single microcrystals in the residue. All examples have nominally similar habits and there are examples of long and short crystals of most in the series.

Author Manuscript Author Manuscript Author Manuscript Author Manuscript

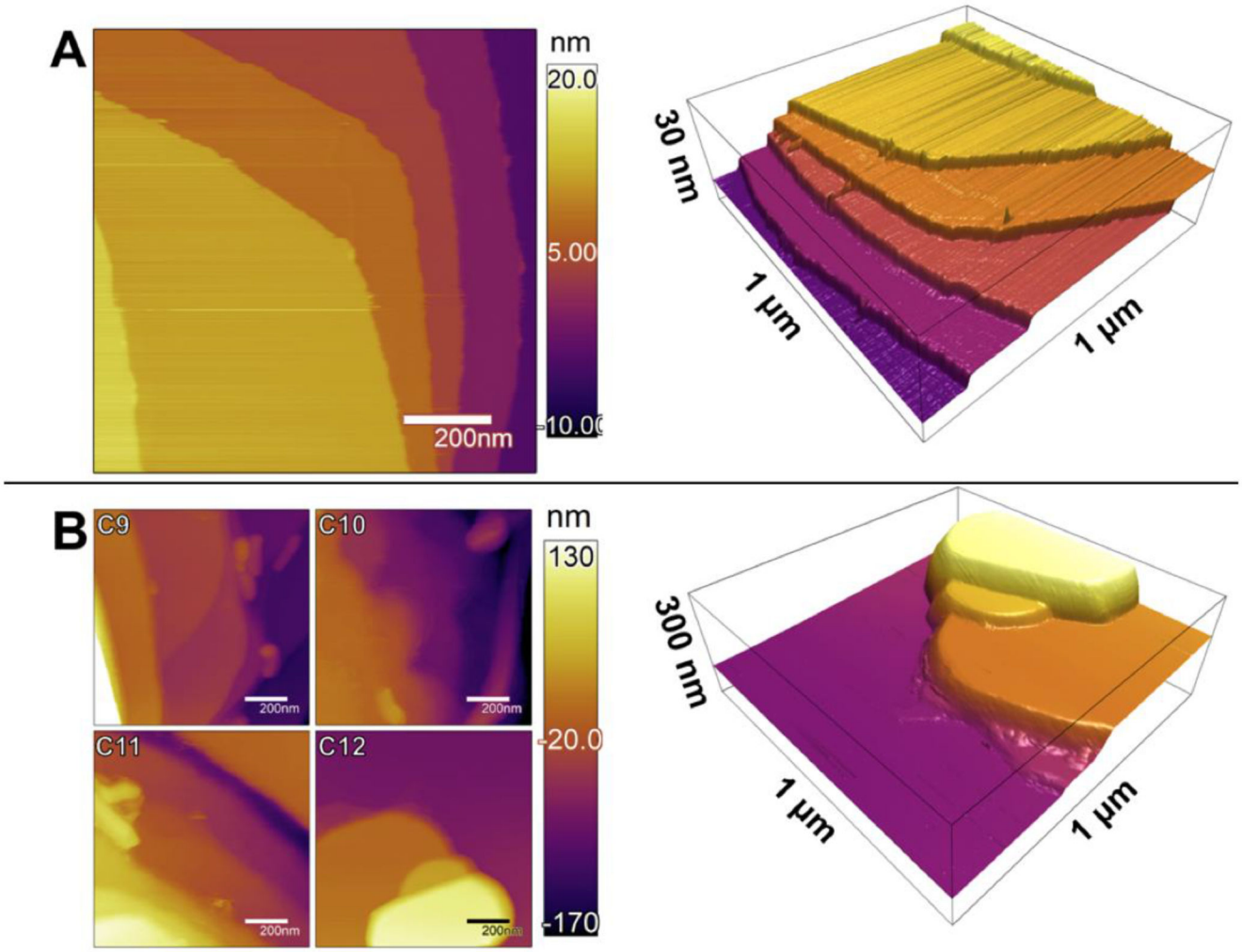

Figure 3:

A) Atomic force topography of a C12 crystal terraces with well-defined molecular step edges and its rendering in 3D. Each terrace presents the methyl terminus of the layers. Surfaces are largely featureless over many microns with no clear evidence of corrugation, vacancies, or domain boundaries. B) An assortment of aggregated crystals from C9-C12. Each is largely featureless on its outermost surface and isolated step edges (as in A) were rare in these samples.

Author Manuscript Author Manuscript Author Manuscript Author Manuscript

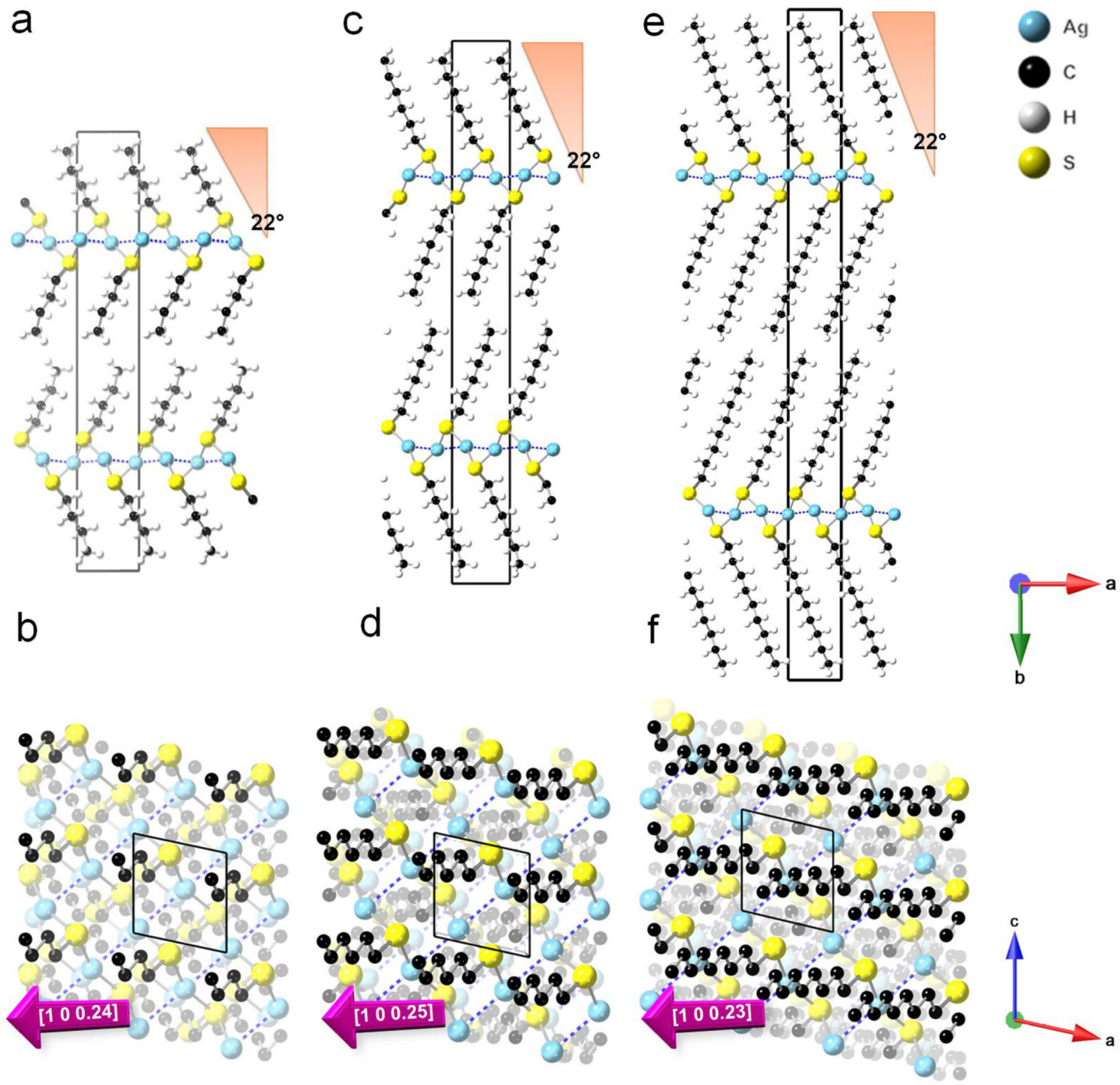

Figure 4:

a,c,e) Cross-sectional views of the C4, C6, and C9 smSFX crystal structures down the *c* axis. The unit cell dimensions are outlined in black. The 22° tilt of the chains from the surface normal direction is conserved across all chain lengths. b,d,f) Viewing the crystals down the *b* axis (view is towards the crystal basal plane) shows the conservation of azimuthal angle and its offset from the principal lattice directions. The purple arrows give the relative orientation of the alkyl chains determined analytically by projecting a vector passing between first and last pairs of carbon atoms onto the *ca* plane. It is approximately parallel to *a**.

Author Manuscript Author Manuscript Author Manuscript Author Manuscript

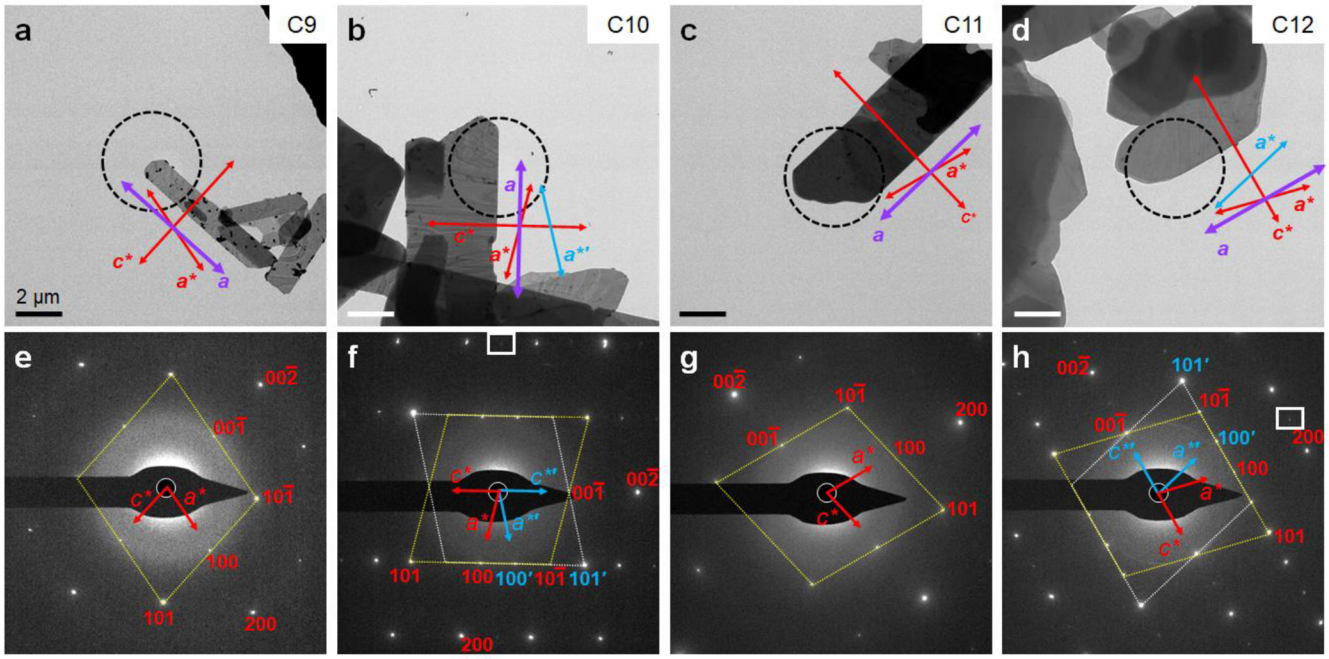

Figure 5:

a-d) Brightfield TEM micrographs and schematics depict the orientation of the principal lattice vectors with the crystal (*a* and *c*: real space vectors, *a** and *c**: reciprocal space vectors. *a* and *a** do not align due to monoclinic symmetry). Assignments were made based on the C9 unit cell. The area in each overlain circle was used for selected-area electron diffraction measurements. e-h) The SAED patterns were indexed using the C9 unit cell as a guide. Both allowed and forbidden reflections are observed in the SAED (e.g. 1 0 0 is forbidden in space group $P2_1/n$). For C10 and C12 (f and h), additional Bragg spots are observed that may be explained by reticular twinning, involving a two-fold rotation about the *a* axis, generating the blue model with primed axes and Miller index numbering (supplemental Fig. S5b). Also, white rectangles highlight extremely faint spots that might indicate *c*-axis doubling (supplemental Fig. S5c).

Author Manuscript Author Manuscript Author Manuscript Author Manuscript

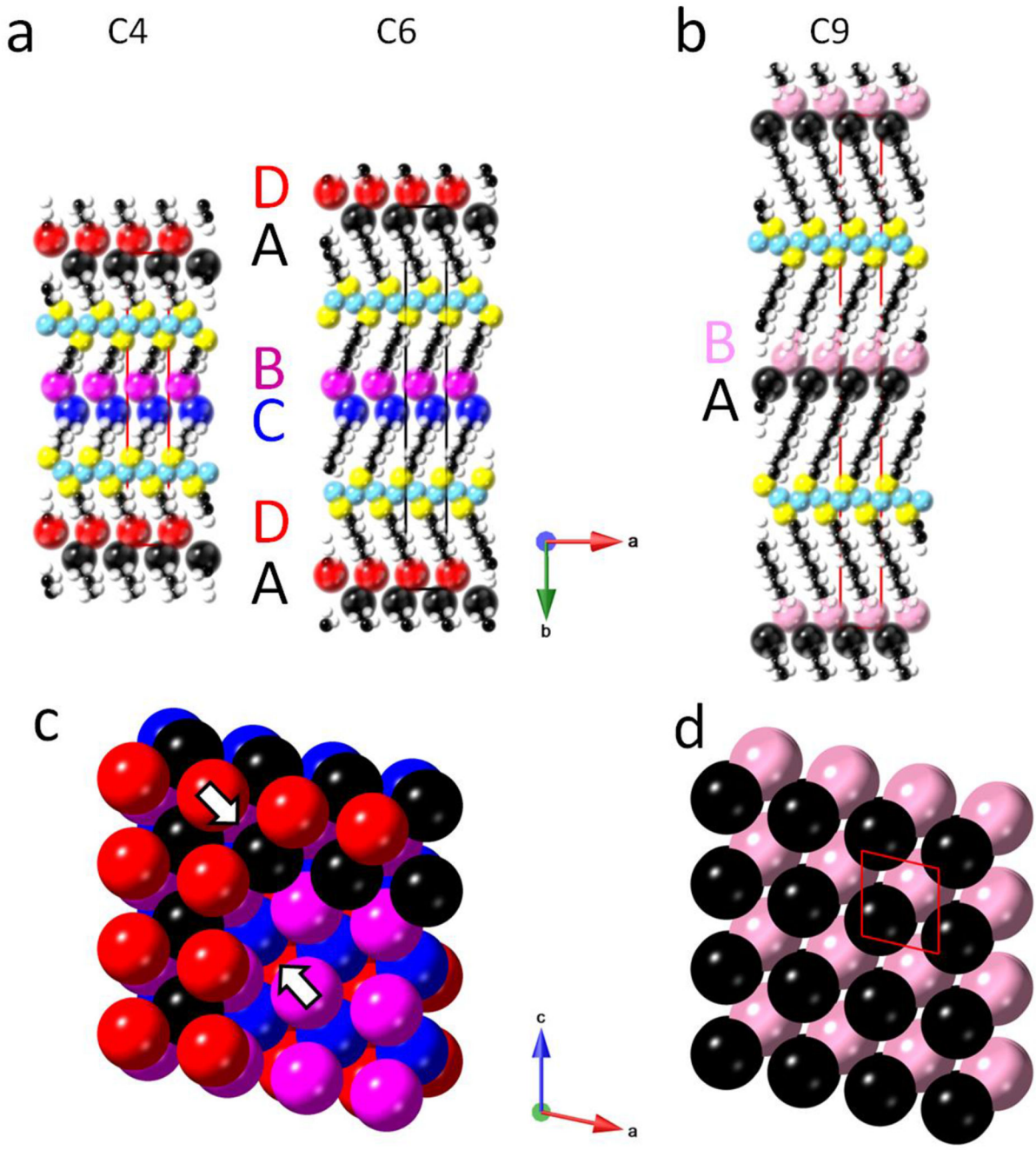

Figure 6:

The odd-even effect in interfacial packing is attributed to differences in packing efficiency at the methyl-methyl interface between layers. Packing patterns are visualized by modeling terminal methyl groups as spheres having a radius of 2 Å that are color-coded by sub-layer. a) Even-numbered alkyl chains in C4 and C6 have a slightly expanded unit cell along the *b* axis relative to the b) odd-numbered C9 system, which is slightly contracted. c) All atoms are hidden except the color-coded methyl groups. Van der Waals contact between a given methyl group and three methyl groups in the next layer creates an effective three-fold hollow

Author Manuscript Author Manuscript Author Manuscript Author Manuscript

(eg. the D/A interface, labeled red and black respectively. The next interface is the B/C interface, labeled purple and blue, respectively. A section of the D/A interface is cut away to reveal B/C. These two interfaces are non-superimposable and there is a small offset between the two interfaces reducing registry. The white arrows indicate the gaps opened by shifting into the 3-fold hollow. d) The methyl groups are well-registered between layers in C9, and the methyl groups are more centered in a 4-fold hollow. Unit cell dimensions are noted as black (even) and red (odd) boxes. Arrows are meant to show the tilt of the various molecules making up each sub-layer.

Author Manuscript

Author Manuscript

Author Manuscript

Author Manuscript

Table 1.

Experimental parameters for all three beamtimes. In this table, OD refers to the diameter of the GDVN liquid exit aperture for P216, LY65, and 3073. EuXFEL repetition rate given as image acquisition rate rather than laser pulse frequency.

Experiment Name	P216	LY65	3073
Facility	LCLS	LCLS	EuXFEL
Instrument	CXI	CXI	FXE
Conditions	Vacuum	Vacuum	Atmosphere
Photon Energy (keV/Å)	10.5/1.18	~18.1/0.686	~15.0/0.827
Beam size (*μ*m)	~1	~1	~20
Repetition Rate (KHz)	0.12	0.12	2
Detector Distance (mm)	~74.9, 108	~60, 160	160, 500
Sample Delivery	ASU GDVN	ASU GDVN	DESY GDVN
Carrier solvent	aqueous surfactant	aqueous surfactant	methanol
Focusing Gas	helium	helium	helium
GDVN aperture OD (*μ*m)	100	100	150

Author Manuscript Author Manuscript Author Manuscript Author Manuscript

Table 2.

Crystallographic data on the three alkanethiolates solved via SFX.

Compound	C4	C6	C9
Formula	$AgSC_4H_9$	$AgSC_6H_{13}$	$AgSC_9H_{19}$
MW	197.04	225.09	267.17
Space group	$P2_1/n$	$P2_1/n$	$P2_1/n$
***a* (Å)**	4.458	4.402	4.404
***b* (Å)**	30.837	40.308	54.075
***c* (Å)**	4.666	4.675	4.743
α (°)	90	90	90
β (°)	101.98	102.43	103.30
γ (°)	90	90	90
V (Å^3)	627.5	810.1	1099.2
Z	4	4	4
ρ_{calc} (g cm^{-3})	2.086	1.846	1.614
XFEL source	EuXFEL	LCLS	LCLS
λ (Å)	0.82656	0.69287	0.69287
T (K)	298	298	298
d_{min} (Å)	0.833	0.833	0.833
μ(mm^{-1})	5.136	2.489	1.847
Frames	3158849	263921	660018
Crystals	26482	3891	24522
Time (min)	26	37	92
Data	1156	1489	2023
Restraints	0	0	0
Parameters	57	74	103
R_1(obs) (%)	10.2	9.6	9.0
R_1(all) (%)	12.0	11.1	9.4
S	1.09	1.09	1.14
Peak, hole (e$^-$ Å^{-3})	1.51, −0.98	1.58, −1.08	3.62, −1.54